

Title	A 3D printed electromagnetic nonlinear vibration energy harvester
Authors	Constantinou, Peter;Roy, Saibal
Publication date	2016-08-24
Original Citation	CONSTANTINOU, P. and ROY, S. (2016) 'A 3D printed electromagnetic nonlinear vibration energy harvester', Smart Materials and Structures, 25(9), 095053 (14pp). doi:10.1088/0964-1726/25/9/095053
Type of publication	Article (peer-reviewed)
Link to publisher's version	10.1088/0964-1726/25/9/095053
Rights	© 2016, IOP Publishing Ltd. This is an author-created, uncopyedited version of an article accepted for publication in Smart Materials and Structures. The publisher is not responsible for any errors or omissions in this version of the manuscript or any version derived from it. The Version of Record is available online at <a href="http://stacks.iop.org/0964-1726/25/i=9/a=095053">http://stacks.iop.org/0964-1726/25/i=9/a=095053</a>
Download date	2024-05-08 19:28:36
Item downloaded from	<a href="https://hdl.handle.net/10468/3225">https://hdl.handle.net/10468/3225</a>

# A 3D PRINTED ELECTROMAGNETIC NON-LINEAR VIBRATION ENERGY HARVESTER

P Constantinou\* and S Roy\*

\*Tyndall National Institute, Cork, Ireland

## Abstract

A 3D printed electromagnetic vibration energy harvester is presented. The motion of the device is in-plane with the excitation vibrations, and this is enabled through the exploitation of a Leaf Isosceles Trapezoidal Flexural pivot topology. This topology is ideally suited for systems requiring restricted out-of-plane motion and benefits from being fabricated monolithically. This is achieved by 3D printing the topology with materials having a low flexural modulus. The presented system has a non-linear softening spring response, as a result of designed magnetic force interactions. A discussion of fatigue performance is presented and it is suggested that whilst fabricating the raster of the suspension element is printed perpendicular to the flexural direction and that the experienced stress is as low as possible during operation, to ensure longevity. A demonstrated power of  $\sim 25\mu\text{W}$  at 0.1g is achieved and 2.9mW is demonstrated at 1g. The corresponding bandwidths reach up-to 4.5Hz. The system's corresponding power density of  $\sim 0.48\text{mWcm}^{-3}$  and normalised power integral density of  $11.9\text{kgm}^{-3}$  (at 1g) are comparable to other in-plane systems found in the literature.

## 1. Introduction

The advent of the Internet of Things predicts that over 25 billion devices by 2020 will be connected together communicating information between each other [1]. Amongst these systems will be remote wireless sensor nodes, potentially part of a wireless network, communicating information about their local environment. However, to fully exploit such systems the nodes need to operate autonomously such that the burden of maintaining batteries is alleviated, or at least reduced. Energy harvesting offers a potential solution to this and is where ambient energy, that is otherwise unused, is extracted from the local environment and converted into useable electrical energy. Within the environment there are a wide range of energy sources that could be harnessed and include thermal, electromagnetic (RF), solar, and mechanical vibrations.

This paper considers a device topology that can harness mechanical vibrations, as they are ubiquitous in the environment and the topology can be fabricated using a 'desktop' 3D printer, exploiting freeform fabrication (FFF) technology. Furthermore the topology is of an 'in-plane' configuration, which is particularly suited to applications where the form factor of the device is required to be thin or flat, and the effect of other vibration modes, in different planes, is undesirable. Out of plane vibration energy harvesters have the implied disadvantage of a larger volume due to the mode they exploit.

Additive Manufacturing (AM) promises to be a disruptive technology and has the potential of revolutionizing manufacturing methodologies where it has been forecasted that the 3D printing industry will exceed \$5B (in US) in 2020, a growth of 300% in comparison to \$1.3B (in US) in 2012 [2]. Currently, in comparison to traditional (subtractive) manufacturing techniques (SM), it is more cost effective to manufacture a small to medium number of

devices, however, post this it becomes beneficial to utilise traditional techniques [2]. However, it promises to be capable of manufacturing unique and complicated topologies, monolithically, unlike traditional techniques.

In this report, an overview of 3D printing technology is presented along with its use in the field of vibration energy harvesting. A review of 'in plane' systems in the literature is then presented followed by the proposed vibration energy harvester topology, where its model and key physical attributes such as suspension and electromagnetic coupling characteristics are discussed. Following this, measurements from a prototype and simulations from a developed model are compared. Finally the system is compared using figure of merits, to similar systems, that are available in the literature.

## 2. 3D printing and Energy Harvesting

### 2.1. 3D printing - general overview

In the 1980's additive manufacturing was originally termed rapid prototyping, where the intent was to provide a fast and cost effective method for creating a prototype. Throughout the product life cycle additive techniques offer many time and cost benefits, in addition to flexibility in design, when comparing to traditional techniques [3]. ASTM International define additive manufacturing as "a process of joining materials to make objects from 3D model data, usually layer upon layer, as opposed to subtractive manufacturing technologies" [3]. Furthermore, additive methods offer the potential benefits of local manufacturing, rapid design iteration and most importantly the elimination of associated costly tooling. Traditional methods (e.g. machining) are subtractive techniques, where assemblies are constructed from a large block of material by removing it. Often, as material is removed this material is lost and wasted. Additive methods, such as 3D printing, can construct a complex functional geometry by

building it layer by layer (on the sub-millimetre scale), thereby conserving material and are able to create a single monolithic assembly. Traditional methods have more complex assembly requirements, however, a wider range of materials can be used in comparison to additive processes [2, 3]. Within additive manufacturing a range of materials can be printed and include, polymers, metals, ceramics, and bio-materials. As a result, there are a wide range of printing applications in a range of industrial sectors.

As outlined in Figure 1 a designer will produce a CAD 3D representation of the proposed device to be manufactured. This is then tessellated and the resulting electronic file is sent to bespoke software where the 3D representation is converted to a number of 2D layers that can then be printed sequentially. The number of layers is typically defined by the printable layer thickness. The printer then prints each layer sequentially, fusing each layer on top of each other.

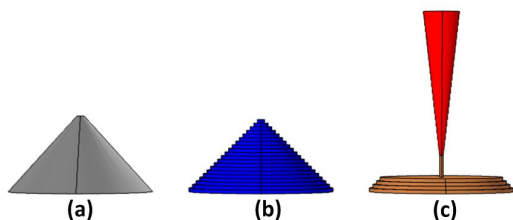


Figure 1: (a) 3D CAD representation (b) sliced version (c) 3D printed version (red – deposition nozzle)

There are at least 13 different technologies which can be grouped into seven different process types [3]. Some of the more common additive manufacturing techniques are listed and compared qualitatively in Table 4. Table 1 lists typical quantitative properties of these technologies.

Table 1: Quantitative Comparison – [ $\mu\text{m}$ ] LR = Low Resolution, SR = Standard Resolution, HR = High Resolution [4]

3D printing Method	Layer Thickness	Minimum Feature Size
SLA	50-100 (HR) 120-150 (SR)	250-380 (HR) 630-890 (SR)
SLS	~100	750-1000
Micro Laser Sintering	2-4	~32
FFF	180 (HR) 250 (SR)	~630
Inkjet (Material)	16 (HR) 30 (LR)	600 (HR) 1100(LR)
Inkjet (Binder)[5, 6]	~100-500	-

## 2.2. Freeform Fabrication

Freeform Fabrication (FFF) systems are common place and are readily available to the consumer market. They typically use thermoplastics to construct the object being printed, which is typically supplied in the form of a thread/filament. Of the available thermoplastics, ABS (Acrylonitrile Butadiene Styrene) and PLA (Polylactic Acid) are the most common. However other thermoplastics, including Nylon

12 or Polycarbonate (PC), are available offering different properties such as greater fatigue strength (Nylon 12 for example), greater strength in tension (PC) and biocompatibility. Their typical material properties (flexural) are compared in Table 2. Their flexural strength and modulus is typically an order lower than that of FR-4 (printed circuit board (PCB) material) and that is an order lower than Silicon. As a result it may be possible to design energy harvesting systems that can harness low frequency vibrations. However, due to the manufacturing process the final object being constructed can be viewed as a laminate composite structure manufactured out of vertically stacked layers. As a result the final mechanical properties of the system do not solely depend on the bulk material properties but also on the print directionality and process (incl. printer quality), producing anisotropic structures [7-9]. Consequently the structure may not be suitable for complex multidirectional loads. The resulting mechanical properties are partially due to the weak inter-fibre fusion between the printed rasters and layers, as well as the resulting porosity of the structures.

As described in Table 4 and in [10] the filament is threaded through a heated nozzle where it is melted and extruded onto a platform or a previously deposited layer where it is fused in the prescribed x-y pattern of the 2D representation of the layer (see Figure 2). If any part of the model requires structural support this is provided by the printer by one of two methods: (i) scaffolding provided by printed ABS material, which is then manually removed post printing (ii) printed layers of soluble material which is dissolved post printing. Once the layer has been printed the platform or the nozzle moves in the 'z' direction and the process repeats.

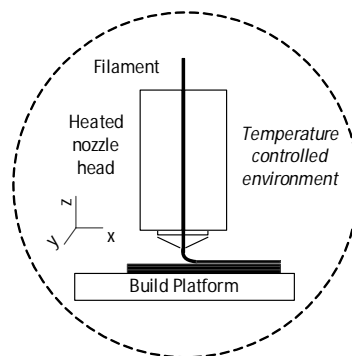


Figure 2: Freeform fabrication process [10]

Table 2: Comparison of flexural properties common FFF materials

	Material	Density [ $\text{gcm}^{-3}$ ]	Strength [ $\text{MPa}$ ]†	Modulus [ $\text{GPa}$ ]†
AM	ABS[11]	1.04	58/35	2.1/1.65
	Nylon 12[12]	1	68.9/59.3*	1.31/1.24*
	PC [13]	1.2	89/68	2.0/1.8
	PLA [14]**	1.24	83	3.8
SM	FR4[15]	1.9	520	21
	Steel	7.85	310	205
	Silicon[15]	2.33	7000	190

\* Unconditioned: direct from FDM machine \*\*Injection molded amorphous bars  
†XZ/ZX

### 2.3. 3D printed Vibration Energy Harvesters

The literature describes several works that utilise additive manufacturing in the context of vibration energy harvesting. Broadly these can be categorised as (a) systems that utilise the technology to manufacture support structures and (b) those systems that manufacture suspension mechanisms using the technology.

Rubes *et al* [16] describe a 3D printed electromagnetic vibration energy harvester, where the suspension is provided by magnetic repulsion and there is a moving magnetic circuit. The fixed components are primarily constructed out of 3D printed ABS and the technology is exploited to manufacture complex geometries. The device has a total volume of  $80 \times 60 \times 60 \text{mm}^3$  and this includes conditioning electronics and housing. A power output of  $26 \text{mW}$  at a DC voltage of  $9 \text{V}$  is generated from an acceleration of  $0.5 \text{g}$  at a resonance frequency of  $17 \text{Hz}$ . In the work they also show that the print direction affects the mechanical properties of the printed ABS. In [17] they further the work, iterating the design and print the structure out of Aluminium and ABS. This prototype has a volume of  $45 \times 55 \times 40 \text{mm}^3$  and weighs approximately  $115 \text{g}$ . It generates a power output of  $127 \text{mW}$  from a high excitation environment. The authors' suggested application is within an aircraft. Bowers and Arnold [18] have used an Inkjet (binder) powder bed printer, as described in the table above, to produce the support structure of their harvester. Their device comprises of a spherical magnetic ball freely moving within a spherical cavity wrapped with coils. The device harnesses human motion and has demonstrated time-averaged power densities of up to  $0.5 \text{mWcm}^{-3}$ . Heit *et al* [19] have presented a harvester comprising of a wishbone spring, supporting a magnetic mass within a 3D printed ABS frame. The spring is made of carbon steel and they have demonstrated that by increasing the separation of the arms of the spring the resonant frequency of the device can be changed. Pillastsch *et al* [20] present a clamp-clamp beam with a freely moving 3D printed mass. They demonstrate that the freely moving mass moves to a position such that the resulting resonant frequency matches that of the driving frequency – this demonstrates a passively self tuning system. There was no transduction mechanism in the system however it is suggested that piezoelectric patches can be used.

In [21] energy is harnessed from a moth. A 3D spring is printed using ABS (FDM (assumed)) and is used as part of an electromagnetic vibration energy harvester that can harness vibrations from the moth. The beam has a folded beam structure which supports a magnet arrangement. Three magnets are arranged along some soft magnetic material and have opposite magnetization directions. Opposite them are another three magnets with the same magnetization directions, such that a 3-pole arrangement is formed. Between each set of magnets is a fixed (relative)

set of coils (3 phase windings) fabricated on a PCB. Through a coil, a load power of  $0.9 \text{mW}$  is reported for a frame excitation of  $0.61 \text{g}$  ( $25.8 \text{Hz}$ ). Inkjet printing [22] has been used to fabricate a non-linear energy harvester with a wide bandwidth. Two PMMA (Polymethyl methacrylate) folded back cantilever beams are fabricated and have magnets placed in their tips. The tips are placed opposite each other such that as they move they actuate each other. A wide (displacement) bandwidth of approximately  $24 \text{Hz}$  is demonstrated at frequencies under  $40 \text{Hz}$ . Energy is converted to the electrical domain utilising piezoelectric patches, and a reported total power of  $18.45 \mu\text{W}$  at a frequency of  $30 \text{Hz}$  is demonstrated. Baker *et al* utilise projection microstereolithography to manufacture energy harvesters [23]. Here a dynamic mask is used to expose curable resin (HDDA – Hexanediol diacrylate) to UV. The process was used to manufacture four helical springs arranged in a  $2 \times 2$  pattern, all of which supported a single magnetic mass. Each spring had a diameter of  $1010 \mu\text{m}$ , a thickness of  $163.5 \mu\text{m}$ , had 2 turns, and a total design height of  $3.4 \text{mm}$ . The magnetic mass passed through a coil, which had 3000 turns made of 48 AWG magnet wire, and a power of approximately  $2.114 \mu\text{W}$  was generated at a frame acceleration of  $0.23 \text{g}$  at a resonant frequency of  $61 \text{Hz}$ .

### 2.4. In-Plane Vibration Energy Harvesters.

The majority of in-plane vibration energy harvesters are predominately electrostatic in nature and exploit an inter-digitated comb drive topology in either an overlapping-area or gap-closing configuration. Fu and Suzuki [24] report an in-plane gap-closing electrostatic energy harvester, with an electret, that has a slightly non-linear softening frequency response and produces a power of approximately  $0.225 \mu\text{W}$  at a frame acceleration of  $1 \text{g}$  and frequency of approximately  $625 \text{Hz}$ . The device layer is  $150 \mu\text{m}$  and the chip size is  $1 \text{cm}^2$ . Nguyen *et al* [25] demonstrate an in-plane overlap varying energy harvester with the same dimensions as [24] and show that it has a softening spring response using an external voltage source to bias the voltage. A generated average power of  $3.4 \mu\text{W}$ , corresponding to a power density of  $226 \mu\text{Wcm}^{-3}$ , is demonstrated at a frame acceleration of  $1 \text{g}$ . With a volume of approximately  $0.042 \text{cm}^3$  Guillemet *et al* [26] demonstrate that an in-plane gap closing electrostatic energy harvester, with trapezoidal fingers, can produce a power of approximately  $2.3 \mu\text{W}$  at a frame acceleration of  $1 \text{g}$ . This corresponds to a power density of  $55 \mu\text{Wcm}^{-3}$ .

There are few electromagnetic and piezoelectric in-plane vibration energy harvesters. Of the piezoelectric topologies in the literature Nadig *et al* [27] report two monolithic micro-machined piezoelectric in-plane bimorph vibration energy harvesters. The first comprises a simple cantilever topology generating a power of  $4.5 \mu\text{W}$  and a power density of  $0.305 \text{mWcm}^{-3}$  at a frame acceleration of  $1 \text{g}$ . The second topology comprises a spiral shaped beam where the

generated power and power density are respectively, at a frame acceleration of 1g, stated to be  $23.14\mu\text{W}$  and  $0.89\text{mW}/\text{cm}^3$ . Fu *et al* [28] report an in plane energy harvester that exploits a mechanical up conversion technique, in response to a low frequency excitation. The device is made of AlN on a Silicon substrate. They show that one of the transducers can generate a peak (instantaneous) power of  $2.27\text{nW}$ .

Typical electromagnetic systems comprise an array of magnets with alternating North-South polarity or Halbach array topologies. These magnet arrangements oscillate above either micro-fabricated or conventionally wound coils. Within the literature there are topologies that are either direct-force driven [29, 30] or comprise of a suspension element and are resonant [31-34]. Chae *et al* [30] demonstrate a magnet arrangement that is spring-less and uses a ferrofluid as a lubricant. A power output of  $71.26\mu\text{W}$  has been demonstrated at an acceleration of 3g and at a frequency of 12Hz. Roundy and Takahashi [29] develop an in-plane harvester using a multi-pole magnetic sheet and PCB coils. Their device generates a peak instantaneous power of  $450\text{mW}$  when the proof mass is displaced by two millimetres and released (12N actuation force). Zhu *et al* [33] present work on a Halbach array suspended by a beryllium copper meander spring, oscillating above copper coils. The reported generated power is approximately  $150\mu\text{W}$  from a frame excitation of 0.5g and resonant frequency of  $\sim 45\text{Hz}$ . Kulkarni *et al* [31] present a micro-fabricated planar device that produces approximately  $150\text{nW}$  at a frame acceleration of 0.45g and resonant frequency of 8080Hz. The device comprises of an electroplated coil on a silicon paddle oscillating in a field formed by two sets of oppositely polarised magnets. Zhang and Kim present two in-plane harvesters [32]. They present a macro-scale system comprising of a large alternating magnetic array and twelve coils. The proof magnetic mass prototype is suspended by plastic springs and has a resonant frequency of 65Hz. The reported power is large ( $11.7\text{mW}$  to  $263\text{mW}$ ), however it is noted that this occurs at an excitation amplitude in the range of 2.1g to 11.2g at the resonant frequency. The reported micro-fabricated device comprising three electroplated coils and a magnetic mass arrangement on a silicon spring generates  $0.2\text{-}2.6\mu\text{W}$  from an excitation of 0.5-3.75g at a resonant frequency of 290Hz. Zhang *et al* [34] continue with the same topology investigating 36 micro-fabricated coils connected together to give over 1000 turns. The coils are multi-layered and are fabricated using through Silicon vias. Multiple coils are stacked and connected using silver paste. Plastic springs are used to suspend a magnet array which move over the coils. A generated power between  $0.7\mu\text{W}$  to  $1.04\text{mW}$  is reported for a frame acceleration between 0.2 to 5g at a resonant frequency of 75Hz.

Mostly the literatures have described topologies that utilise 3D printing to fabricate the suspensions of vibration energy harvesters, where their principal mode of vibration is out of plane. Of the in-plane systems, electrostatic systems dominate, however these are confined to MEMS scale devices (low power) as well as requiring an external voltage source. Piezoelectric systems are prone to depolarization, generate a low current when the material is strained, and become brittle over a large number of cycles of vibrations. Electromagnetic systems can generate current at a higher level and do not require an external voltage source. This paper presents a novel 3D printed electromagnetic vibration energy harvester that addresses an in-plane operation requirement, and exploits the low flexural modulus of ABS, in a particular non-linear configuration, to increase the system power and bandwidth at relatively lower frequencies.

### 3. Topology Configuration and System Model

#### 3.1. Topology

The proposed topology in the present work is as shown in Figure 3. The suspension consists of two ABS printed beams attached to a base and to a support platform that is allowed to move. The platform holds two magnets whose magnetization directions are anti-parallel ( $180^\circ$  out of phase). Opposite to the two magnets another set of two magnets is fixed to the frame arranged in the same orientation. Between the pair of magnet sets a coil is placed, attached to the same frame as the stationary magnets and beam suspension base. As the frame is excited the suspended magnets move and the coil experiences a change in magnetic flux linkage which results in an induced voltage, and an induced current when a load is attached to the coil. The motion of the magnets is in plane to the suspension and excitation vibrations. As a result of the restoring force, the system will have a resonant frequency response and operating at the resonant frequency is the condition for maximum energy transfer from the mechanical to electrical domain, according to classical vibration energy harvesting theory [35]. The restoring force ( $f_{res}$ ) comprises both mechanical and magnetic components. The mechanical component is a result of the beam suspension mechanism and the magnetic component is due to the magnetic force interaction between the moving and stationary magnets. The latter is non-linear and yields a system frequency response that is of a harvester with a softening spring suspension, based on the present orientation of the magnets.

The topology described above is akin to a Leaf Isosceles Trapezoidal Flexural (LITF) pivot, a type of complex flexure, as described in [36]. Flexural pivots are commonly used in a wide range of applications such as precision engineering, metrology and aerospace [36, 37]. Their benefits include

reduced weight, motion smoothness, are frictionless and lubrication free. In addition, they can be fabricated monolithically, making additive manufacturing an ideal candidate to develop such systems. These systems are suited for in-plane motion where their in-plane compliance is lower in comparison to that of their out-of-plane dynamics [37]. This is a result of the thickness of the spring architecture.

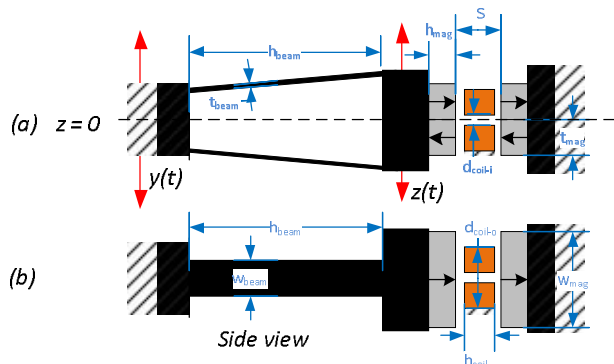


Figure 3: (a) Top view (b) Side view

In the literature FR-4 has been used to achieve a low resonant frequency with out-of-plane vibration systems. Examples of systems utilizing FR-4 include those described in [15, 38-41]. Typically, a topology made of this material is fabricated using either a CNC machine or laser micro-machine. A 3D monolithic topology, such as the LITF, cannot be fabricated easily utilising laser micro-machining and FR-4 as the thickness through which a laser can cut through within tight tolerances is restricted to a less than a millimetre.

The use of 3D printing technology will allow a complex 3D flexural pivot topology to be fabricated monolithically as a single process, alleviating many of the fabrication concerns, associated with traditional methods. If a low flexural modulus is desired for the system, thermoplastics can be used readily in 3D printing manufacturing. Table 3 compares the eigen frequency of the first mode (in plane) of the proposed topology in three different mediums. It shows that ABS offers the lowest frequency of the materials. Furthermore, to achieve the same frequency as the system fabricated in ABS using FR-4 or steel this would require fabricating thinner beams in these materials, further complicating the manufacturing process.

Table 3: Comparison of in-plane frequencies

	ABS	FR4	Steel
Frequency [Hz]	117	338	689
Flexural Modulus [GPa]	2.1	22	205

### 3.2. General Model

The analysis that follows utilises the physical and material properties of the prototype evaluated in section 4, and are listed in Table 5 unless otherwise stated. The prototype can

be modelled through the following equations and has been represented as a time-step model in MATLAB/Simulink:

$$m\ddot{z}(t) + c\dot{z}(t) + f_{res}(z(t)) = -m\ddot{y}(t) \quad (1)$$

$$m\ddot{z}(t) + c\dot{z}(t) + \frac{dU(z(t))}{dz} = -m\ddot{y}(t) \quad (2)$$

$$c = c_m + c_e(z(t)) \quad (3)$$

$$c_e(z(t)) = \frac{(k_{e-total}(z(t)))^2}{\sqrt{(R_C + R_L)^2 + (\omega L_C)^2}} \quad (4)$$

where  $m$  is the equivalent mass of the beam, support and magnets;  $c$  is the total viscous damping;  $z$  is the relative displacement from the centre position (neutral position,  $z = 0$ );  $c_m$  is the viscous mechanical damping (can be derived experimentally from open circuit measurements);  $c_e$  is the equivalent electrical damping and is a function of displacement;  $k_e$  is the electromagnetic coupling coefficient and is a function of displacement;  $R_L$  is the load impedance (here assumed resistive);  $R_C$  is the coil resistance;  $L_C$  is the coil inductance;  $\omega$  is the frequency of excitation;  $y$  is the frame excitation displacement; and  $U(z)$  is the restoring force potential as a function of  $z(t)$ .

### 3.3. Restoring Force

The restoring force ( $f_{res}$ ) comprises of two components: the linear mechanical contribution due to the suspension topology and the non-linear contributions due to the magnetic force interaction between the moving and fixed magnets.

#### 3.3.1. Suspension Force

In order to determine the contribution of the suspension topology Finite Element Analysis (FEA) was conducted in COMSOL. The first three eigen modes due to the suspension are shown in Figure 4 and comprise of an in-plane, out-of-plane and torsional mode.

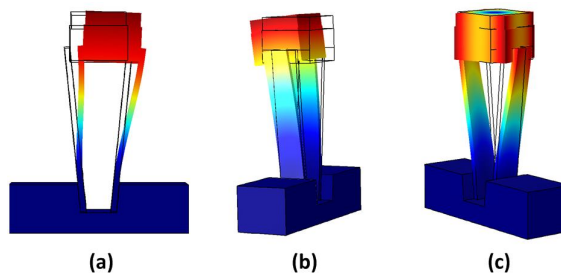


Figure 4: Eigen modes (a) In plane (b) out of plane and (c) torsional

As discussed previously the mechanical properties of 3D printed materials can vary between systems, and printed orientation. Typically the accuracy of the printed part will depend on the print raster orientation, the part size and geometry. The eigen frequencies due to  $\pm 0.05\text{mm}$  wall thickness deviation from the required dimension (here

**Table 4: A qualitative comparison between common 3D printing techniques [3, 42]**

<b>Technology</b>	<b>Process Description</b>	<b>Typical Materials</b>	<b>Advantages</b>	<b>Disadvantages</b>
<b>Stereo-lithography (SL)</b>	<i>A laser scans an X-Y cross section of the 3D object to be printed on the resin and it cures and solidifies.</i>	Liquid photopolymers and composites.	<ul style="list-style-type: none"> <li>• Complex geometries.</li> <li>• Detailed Parts.</li> <li>• Smooth finish.</li> </ul>	<ul style="list-style-type: none"> <li>• Post processing required (cleaning and curing).</li> <li>• Requires support structures for overhangs and undercuts.</li> <li>• Stability of material over time (UV exposure).</li> </ul>
<b>Laser sintering (LS)</b>	<i>A laser scans an X-Y cross section of the 3D object to be printed on a powdered bed sintering/melting the material forming a solid object.</i>	Powdered: paper, plastic, metal, glass, ceramic, composites.	<ul style="list-style-type: none"> <li>• Requires no support structures due to powder bed.</li> <li>• High heat &amp; chemical resistance.</li> <li>• High speed.</li> <li>• Stronger material properties to SL.</li> </ul>	<ul style="list-style-type: none"> <li>• Accuracy limited to powder particle size and poorer to SL.</li> <li>• Rough surface finish relative to SL.</li> <li>• Porosity issues (requiring infiltration of other materials).</li> <li>• High in process temperatures and long cooling times.</li> </ul>
<b>Freeform Fabrication (FFF) or Fused Deposition Modelling (FDM, Stratasys™)</b>	<i>A plastic filament is melted and deposited via a heated extruder to form a 2D image on an X-Y plane. Melted plastic hardens when cooled.</i>	Thermoplastics.	<ul style="list-style-type: none"> <li>• Strong Parts.</li> <li>• Complex geometries.</li> </ul>	<ul style="list-style-type: none"> <li>• Poorer surface finish (relative to SL).</li> <li>• Slower build times (relative to SL).</li> <li>• Support structures required.</li> <li>• Permeable structures.</li> </ul>
<b>Inkjet (Material)</b>	<i>Material is jettisoned in an X-Y pattern and then hardened, for example in the case of a photopolymer, with UV light.</i>	Photopolymers and wax.	<ul style="list-style-type: none"> <li>• Good accuracy.</li> <li>• Good surface finish.</li> <li>• Multiple material use.</li> <li>• Hands free removal of support material.</li> </ul>	<ul style="list-style-type: none"> <li>• Relatively slow process.</li> <li>• Limited wax materials.</li> </ul>
<b>Inkjet (Binder)</b>	<i>A binder is deposited onto a powdered bed in an X-Y plane pattern, and fuses the material together</i>	Ceramic powders, metal laminates, acrylic, sand, composites.	<ul style="list-style-type: none"> <li>• Full colour models.</li> <li>• Inexpensive.</li> <li>• Fast to build.</li> <li>• No supports required to build overhangs and undercuts.</li> </ul>	<ul style="list-style-type: none"> <li>• Limited accuracy.</li> <li>• Poor surface finish.</li> <li>• Not as strong as SL.</li> <li>• Requires post processing to ensure durability.</li> </ul>

**Table 5: Physical and Material properties**

Property	Symbol	Value
Beam Height	$h_{beam}$	17.8[mm]
Beam Thickness	$t_{beam}$	0.8[mm]
Beam Width	$W_{beam}$	4[mm]
Flexural Modulus [ABS]	$Y$	2.1[GPa]
Density [ABS]	$\rho_{ABS}$	1040[kgm <sup>-3</sup> ]
Coil Outer Diameter	$d_{coil-o}$	6.5[mm]
Coil Inner Diameter	$d_{coil-i}$	1.15[mm]
Coil Height	$h_{coil}$	2[mm]
Number of turns	$n_{tot}$	7060
Gauge	$g$	25 $\mu$ m
Coil Resistance [measured]	$R_c$	3.287k $\Omega$
Coil Inductance [measured]	$L_c$	196mH
Magnet Width	$w_{mag}$	8[mm]
Magnet Thickness	$t_{mag}$	4[mm]
Magnet Height	$h_{mag}$	2[mm]
Separation between magnets	$S$	4[mm]
Magnetic Remanence	$B_r$	1.17[T]
Density [NdFeB]	$\rho_{NdFeB}$	7400[kgm <sup>-3</sup> ]
Mass of suspension and magnets [calculated]	$m$	1.42g
Eigen frequency [in plane]	$\omega_n$	116.8[Hz]
Eigen frequency [out plane]	-	259.2[Hz]
Eigen frequency [torsional]	-	742.1 [Hz]

0.8mm) results in a  $\pm 10.5$ Hz deviation in the in-plane (116.8Hz),  $\pm 7.5$ Hz out-plane (259.2Hz) and  $\pm 30$ Hz torsional (742.1Hz) eigen frequencies. The latter two modes are at relatively higher frequencies as a result of the LITF topology and hence this topology is suitable for in-plane vibration energy harvesters.

The suspension force is determined from the first mode (in-plane) eigen frequency,  $\omega_n$  and the equivalent mass of beam, support platform and magnets,  $m$ :

$$f_{susp}(t) = z(t)k_{susp} = z(t)m\omega_n^2 \quad (5)$$

where  $k_{susp}$  is the mechanical spring constant.

### 3.3.2. Magnetic and Total Restoration Force

As the magnets move the experienced magnetic force changes from an attractive form, when  $z = 0$ , to a repulsive form. The corresponding total restoring force is shown in Figure 5 along with the corresponding potential profiles, in Figure 6, where the potential,  $U(z)$ , is given by:

$$f_{res}(z) = \frac{dU(z)}{dz} \quad (6)$$

The variation of the force and potential, versus separation between the moving and fixed magnets about the neutral position ( $z = 0$ ) shows the potential profile is that of a mono-stable nonlinear device. It shows that as the separation,  $S$ , decreases the motion becomes harder for the moving magnet to move as the gradient of the potential well becomes steeper. This is because the pairs of magnets are closer together and hence the attractive

force between the two pairs becomes stronger, as the gap decreases.

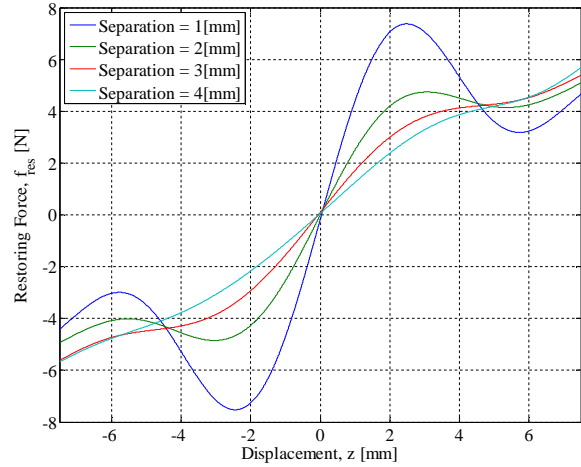


**Figure 5: Restoring force as a function of displacement**

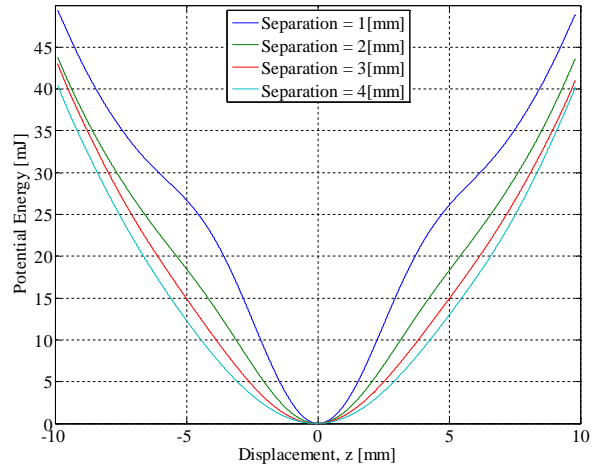


**Figure 6: Potential energy profile as a function of displacement**

### 3.4. Electromagnetic Coupling Coefficient

The magnetic flux distribution is as shown in the figure below and is that of an anti-parallel configuration (magnetic vectors of top and bottom magnets are 180° out of phase with each other). Shown are two topologies (A&B) where soft magnetic material is used in topology B to constrain the magnetic flux, resulting in an increase in the electromagnetic coupling coefficient. The electromagnetic coupling coefficient determines how well the electrical and mechanical domains of the system are linked and hence how much energy can be transferred between the domains.

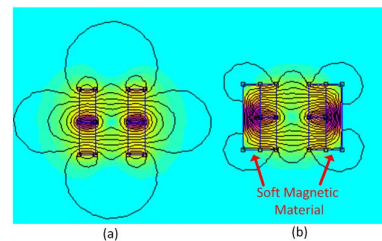


**Figure 7: Magnetic flux distribution for topology (a) and (b) B**



It is given by Faraday's law of electromagnetic induction where the open circuit voltage,  $v_{oc}$ , is given by:

$$\begin{aligned} v_{oc}(t) &= -\dot{z}(t)n_{tot} \frac{d\phi_{avg}(z(t))}{dz} \\ &= -\dot{z}(t)k_{e-total}(z(t)) \end{aligned} \quad (7)$$

where  $\phi_{avg}$  is the average flux through the coil,  $z$  is the relative displacement between the moving magnets and fixed coil, and  $k_{e-total}$  is the system electromagnetic coupling coefficient. The corresponding electromagnetic coupling coefficient for the two topologies is as shown in Figure 8, assuming the coil in the prototype is used, along with another topology where both sets of magnets are moving (Topology C). It shows that with reference to Topology A that there is ~30% increase in the coupling coefficient (at the neutral position) with Topology B and similarly with Topology C ~100% increase is observed.

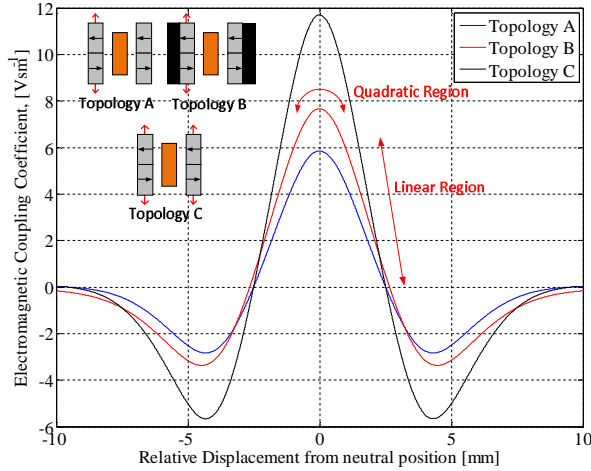


Figure 8: Corresponding electromagnetic coupling coefficient

A modulated induced voltage is a result of the displacement dependent electromagnetic coupling coefficient. When the system operates (under the assumption of harmonic motion) in a region where the coupling is linear the voltage comprises of 1<sup>st</sup> and 2<sup>nd</sup> order harmonics, as described in [43]. When the system is operating around the turning points of the profile the coupling can be modelled as a quadratic function of displacement. As a result, the voltage will comprise of 1<sup>st</sup>, 2<sup>nd</sup> and 3<sup>rd</sup> order harmonics. The voltage for these regions can be described by the following equations:

$$v_c(t)|_{general} = Z\omega \cos(\omega t) [f(Z\sin(\omega t))] \quad (8)$$

$$v_c(t)|_{linear} = Z\omega k_e(Z_o) \cos(\omega t) + \frac{\beta_{reg}Z^2\omega}{2} \sin(2\omega t) \quad (9)$$

$$\begin{aligned} v_c(t)|_{quad} &= \left( Z\omega k_{e-max/min} \mp Z(Z_o - Z_{max})^2\alpha\omega \right. \\ &\quad \left. \mp \frac{\alpha\omega Z^3}{4} \right) \cos(\omega t) \mp \alpha Z^2\omega(Z_o \\ &\quad - Z_{max})\sin(2\omega t) \\ &\quad + \frac{\alpha Z^3\omega}{4} \sin(3\omega t) \end{aligned} \quad (10)$$

where  $Z_o$  is the initial position,  $Z$  is the amplitude of oscillation,  $\beta_{reg}$  is the gradient of the electromagnetic coupling in the linear region,  $Z_{max/min}$  is the maximum relative displacement from the rest position and  $\alpha$  is the coefficient of the quadratic relationship.

For the proposed prototype, the system operates around the neutral position where a turning point in the electromagnetic coupling coefficient exists. At an acceleration of 1g, and at an excitation frequency of approximately 150Hz, the following figure shows the FFT of the open circuit voltage (from measurements) and that it is dominated by 1<sup>st</sup>, 2<sup>nd</sup> and 3<sup>rd</sup> order harmonics, corresponding with the quadratic approximation given by the equation above. Higher order harmonics do exist as the motion of the moving magnet arrangement is beyond the region of which the quadratic region is valid.

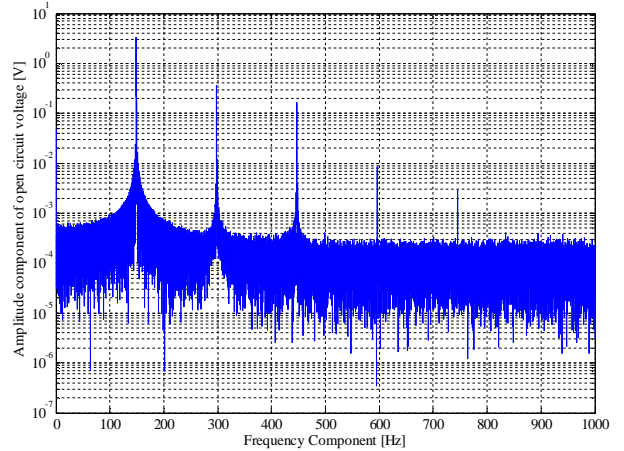


Figure 9: FFT of recorded open circuit voltage

## 4. Experimental Evaluation and Model Evaluation

### 4.1. Prototype and test set up

The proposed topology (Figure 10) was fabricated using a Stratasys Mojo 3D printer, which uses FDM technology, out of ABS. The raster direction of the beams was printed perpendicular to the flexural direction to ensure the material's properties were as close to the bulk properties. Sintered NdFeB (grade N35) permanent magnets were glued to the frame and support platform and a coil (Recoil Ltd., Kent, UK) was fixed to the frame and placed between the magnets with an air-gap of 1mm between itself and both pairs of magnets. The coil had approximately 7060 turns, had a gauge of 25 $\mu$ m, had an air core, was scramble wound, had skeined ends for added handling strength and

its measured coil properties are listed in Table 5, along with its other physical properties.

The method of winding will contribute to the number of turns that can be wound in a cross sectional area of a coil and is typically characterised by the packing factor, PF, the total cross sectional area of the coil turns to that of the area they occupy. This affects the electrical properties of the coil as well as the number of turns and hence induced voltage. In a scramble wound coil the position of the wire is not precisely controlled and the layers may not be completed before the next one is started during winding. Typically their packing factors lie between  $PF = 50-60\%$ . For the coil used in the prototype a  $PF \approx 65\%$  is calculated. In contrast, orthogonal wound coils have a packing factor of approximately  $PF = 78\%$  and is where the coil turns sit directly on top of each other. Orthocyclic wound coils is where the wire of alternating layers sit in the grooves between two coil turns of the previous layer yielding a packing factor of up to  $PF = 90\%$ . However, the latter two are challenging to fabricate [44].

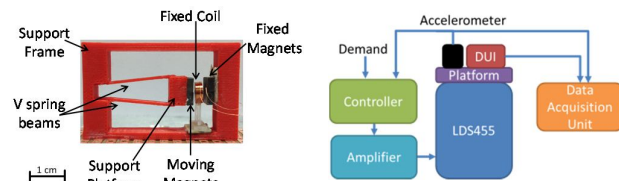


**Figure 10: (a) Photograph of prototype (b) Block diagram of experimental setup; DUI –Device Under Investigation**

The prototype was evaluated on an LDS455 dynamic shaker with a closed loop controller, as depicted in Figure 10 (b). Both the induced voltage and base acceleration, the latter as a reference, were recorded using a computer based oscilloscope. All measurements were in the form of both up and down frequency sweeps in the range from 100Hz to 200Hz, at a rate of 1Hz/s.

#### 4.2. Open Circuit Measurements

Typical measured and calculated open circuit frequency responses are shown in Figure 11 and show that an open circuit  $Q$  factor of  $Q = 100$ , which corresponds to a mechanical damping ratio of  $\zeta_m = 0.005$ , provides a good empirical fit to the measurements.

From the figure, it is clear that the frequency response is of a softening spring type, and the bandwidth of the device increases between the up and down sweeps. Nguyen and Halvorsen [45] report that softening springs yield a higher average power output in comparison to hardening or linear spring systems when excited by white noise vibrations. The degree of nonlinearity will affect the power output and it has been shown that softening springs can produce a wider bandwidth than linear or hardening spring systems under the same conditions. For sinusoidal sweeps the bandwidth of hardening springs increases as the magnitude of the vibration increases, and is wider for up sweeps, increasing

towards higher frequencies. In contrast the bandwidth of softening spring systems increase towards lower frequencies during down sweeps.

The measured and calculated resonant frequencies of the open circuit voltage differ slightly and this may be attributed to the variability in the printed beam thickness due to the manufacturing tolerances. Figure 12 shows the peak open circuit voltage, peak frequency and bandwidth as functions of frame acceleration. The measurements fall favourably with the calculations (from the model described above) exhibiting the same trends. The peak voltage increases and the peak frequencies decrease with increasing frame acceleration. The voltage at which the bandwidth is calculated for both the up and down sweeps is the half peak voltage of the up sweep and increases with acceleration. At low accelerations the bandwidth is approximately the same for both up and down sweeps, where a bandwidth of approximately 2Hz is determined. However, at higher frame accelerations the bandwidth is greater. A moderate increase to approximately 2.5Hz is observed for the up sweep at 1g and an approximate value of  $\sim 4.75\text{Hz}$  is calculated and measured at just under 6.5Hz for the down sweep.

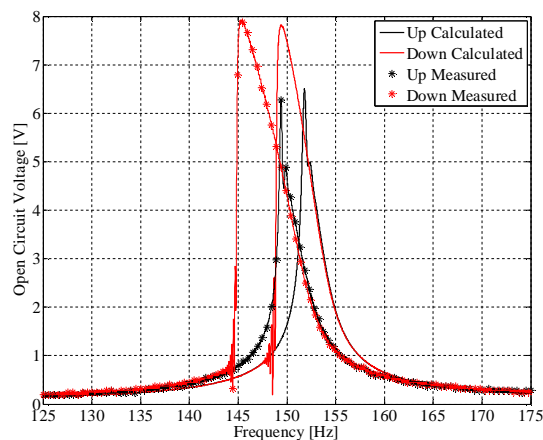


**Figure 11: Up and down frequency sweeps of the peak open circuit**

#### 4.3. Power Measurements

Figure 13 shows the peak power of the system as a function of resistive load, for a frame acceleration of 1g. Figure 13 (b), and Figure 13 (c) respectively show the corresponding peak frequency, at which the maximum occurs and the corresponding bandwidth of the frequency sweep.

As the frame acceleration increases the magnitude of the peak power (note the average of up and down sweeps is listed here) increases from  $25\mu\text{W}$  at 0.1g to 0.7mW at 0.5g and 2.5mW at 1g (at  $R_L = 7k\Omega$  (downsweep)), corresponding to an approximate increase proportional to the square of the frame acceleration. The power level at which the bandwidth, for both up and down sweeps, was determined as that of the half power of the up sweep

response. At a frame acceleration of 1g the bandwidth of the down sweep increases and that of the up sweep decreases with load. Observations at lower accelerations show that the bandwidth decreases with both down and up sweeps. The peak frequency remains relatively similar across all loads except for a frame acceleration of 1g where it is shown to decrease during the down sweep when the load is increased. At this frame acceleration a maximum bandwidth of just under 4.5Hz is demonstrated during the down sweep. During the up sweep the maximum bandwidth is shown to be approximately 2Hz at a load of approximately 1k $\Omega$ . The differences between the up and down sweep measurements are a result of the system's non-linearity, and this becomes more prominent as the frame acceleration increases.

#### 4.4. Stress and Fatigue Analysis

The fatigue lifetime is dependent on the stress experienced by the suspension element and the material's flexural strength. To ensure a certain lifetime criterion it is important to assess whether the displacement (hence stress) of the suspension element does not exceed a certain limit under the desired operating conditions.

The maximum stress is exhibited at the ends of the suspension elements and it increases with tip displacement. The tip displacement is a maximum during down sweeps and is proportional to the system damping and frame acceleration. By increasing the damping in the

system, the tip displacement can be restricted. Hence, when a load is applied, the damping in the system increases as energy is extracted from the mechanical to electrical domain. As a result the displacement of the mover is reduced and it can be shown to increase with load. As there is an optimal load resistance for which maximum power transfer occurs, it can be shown that a large displacement does not always imply a larger generated power. As discussed in the literature [7, 10] the raster print direction will affect the flexural strength (note indications to the flexural strength can be drawn from the available tensile fatigue data) and it can be concluded that a suspension element should be printed with its rasters perpendicular to the flexural mode (as in this case the material properties more closely emulate that of the bulk material) and the maximum stress should lie at a sufficiently low percentage of the flexural strength (e.g. < 10-20%) to ensure longevity.

For the prototype under consideration, the flexural strength of ABS is approximately 60MPa, therefore operating the system with a maximum stress of 6-12MPa will help ensure longevity. This corresponds to a displacement of approximately ~0.4-0.8mm, and with reference Figure 14, will allow operation at < 0.36-0.73g under optimally loaded operation. This corresponds to a peak power generation of ~0.28-1.28mW.

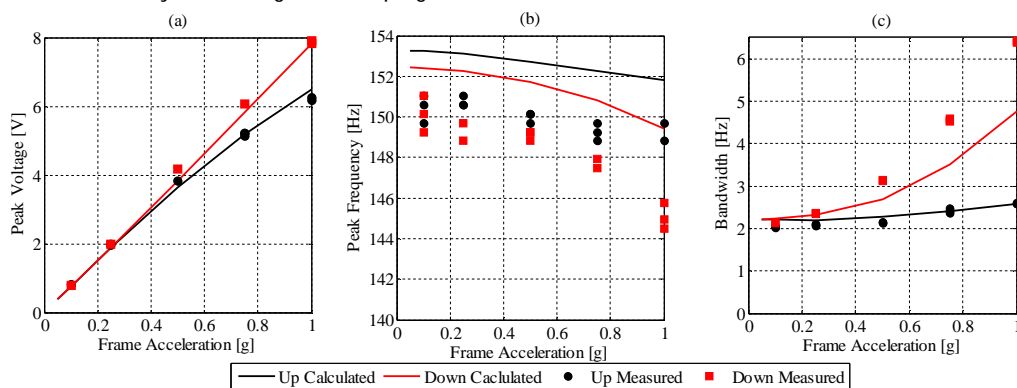


Figure 12: Corresponding (a) peak open circuit voltage, (b) peak frequency and (c) bandwidth as a function of frame acceleration

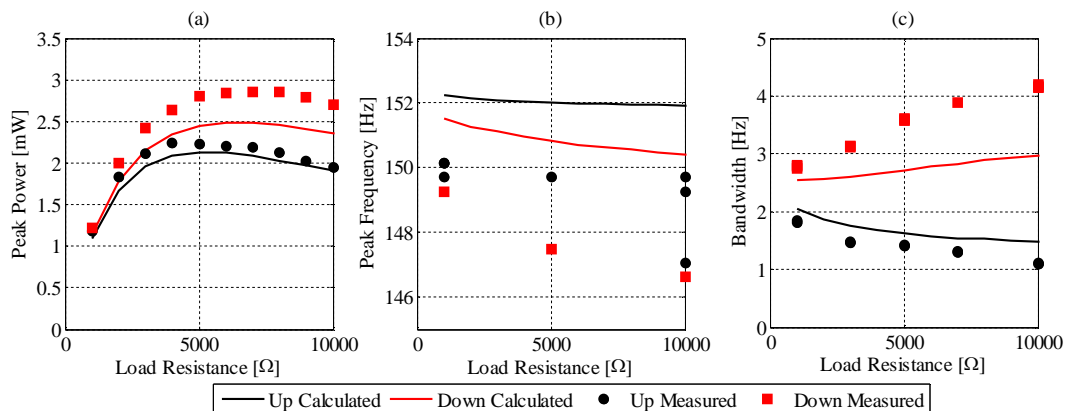
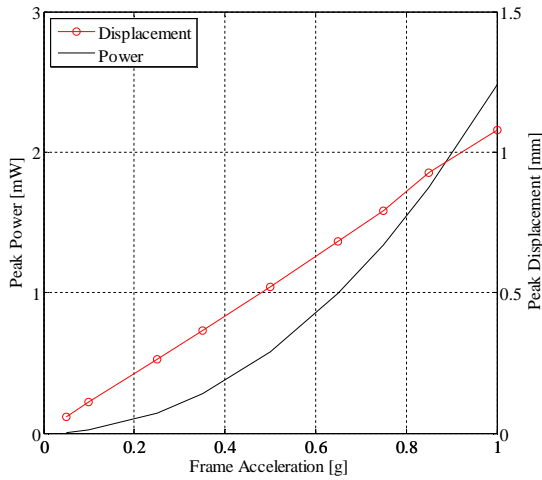


Figure 13 : (a) Peak Power (b) corresponding peak frequency (c) corresponding bandwidth vs load



**Figure 14: Frame acceleration vs peak power and corresponding peak displacement.**

## 5. System Benchmarking

There are a number of metrics outlined in the literature that can be used to benchmark the system described here. Of the metrics utilised in this paper the volumetric power density, is given by:

$$PD = \frac{P}{\mathcal{V}} \quad (11)$$

where  $\mathcal{V}$  is the volume of the device under consideration. In addition to this metric, the 'Normalised Power Integral Density' (NPID), as described in [38] is used to incorporate the importance of the bandwidth of the system in a nonlinear device and it is given by:

$$NPID = \frac{\int_{f_1}^{f_2} P df}{\mathcal{V} \dot{y}^2} \quad (12)$$

where  $f_1$  and  $f_2$  are the lower and upper extremities of the bandwidth.

Table 6 lists and compares the metrics for different devices outlined above. In terms of NPID some electrostatic systems can produce large values and this is largely due to their large bandwidth and small volume, as they are typically MEMS devices. However, due to their small volume they produce power in the order of micro-watts and are typically constrained by the need of an external voltage source to operate. Of the piezoelectric in-plane systems PD are larger (for the most part) than those reported for electrostatic systems and similarly produce power in the order of micro-watts due to their small volume. In comparison to electromagnetic systems the PD is better than those of the MEMS devices however, generally piezoelectric systems generate a low current when the material is strained and can be brittle.

On comparing the NPID of the electromagnetic systems the prototype NPID ( $5.3\text{kgm}^{-3}$ ,  $6.95\text{kgm}^{-3}$  and  $11.9\text{kgm}^{-3}$  at 0.1g, 0.5g and 1g respectively) compares well to other systems, and better than that of the device exploiting a Halbach array topology [33] ( $1.49\text{kgm}^{-3}$  at 0.5g). It performs

better than the 3D printed system [23] ( $2.52\text{kgm}^{-3}$  at 0.23g) that operates out of plane. However [31] demonstrates a larger NPID largely due to the system's high bandwidth and small volume, yet generates a low power due to its size. On comparing the PD of the electromagnetic systems the prototype performs similarly (or better) with a density of  $0.48\text{mWcm}^{-3}$  (at 1g). In comparison to the macro system presented, its PD, at 1g, is superior than the macro system's PD, at 2.1g, which is  $0.45\text{mWcm}^{-3}$ . The volume of the macro scale device is  $26\text{cm}^3$  and that of the prototype is  $6\text{cm}^3$ .

The prototype that has been developed generates a maximum power of 2.9mW at a frame acceleration of 1g (at  $R_L = 7k\Omega$  (downsweep)). In addition, the device has been fabricated monolithically, exploiting FDM technologies. The LITF topology restricts out of plane modes to higher frequencies enabling an in-plane system to be exploited. However, the performance of the topology can be improved. As discussed earlier, the incorporation of soft magnetic materials will increase the electromagnetic coupling coefficient and a corresponding increase in the generated power will be observed. However increasing the proof mass will decrease the resonant frequency, yet this may be a benefit if this is desired. Allowing both sets of magnets to move will increase the electromagnetic coupling further. This can be achieved by either moving the magnets as a single unit, or allowing the magnet sets to move separately on separate suspension mechanisms. The former will behave linearly yet the latter will perform non-linearly when the magnet pairs move out of phase, resulting in a wider bandwidth. This phase difference may be achieved by manipulating the beam and mass design. In addition, in the case of the latter the volume of the device increases due to the additional suspension. The frequency response of the system is of a softening spring type, which is more suitable for white noise vibration harnessing. The bandwidth of the prototype is approximately 4.5Hz at a frame acceleration of 1g, however, this can be improved by exploring different mechanisms that enhance the systems non-linear properties, which would yield a broad frequency response.

## 6. Summary

This paper has outlined the development of a non-linear in plane electromagnetic vibration energy harvester fabricated using 3D printing. 3D printing offers the potential of rapid development; cost savings and the capability of manufacturing relatively complex topologies monolithically eliminating any issues associated with conventional manufacturing such as assembly.

The in-plane response is derived from a topology akin to the Leaf Isosceles Trapezoidal Flexural Pivot which restricts out of plane motion. The topology itself is well suited to 3D printing as conventional methods are restrictive or the

topology cannot be achieved using alternative materials (e.g. FR-4) and conventional methods of fabrication.

A non-linear frequency response is achieved through the introduction of a moving vs fixed magnet arrangement. The response is of a softening spring, which is more suitable to harnessing white noise vibrations than linear or hardening spring systems. The measured and calculated results are comparable and any discrepancies can be attributed to manufacturing tolerances and the empirical determination of the mechanical damping.

The prototype has yielded a power of 2.9mW and bandwidth of 4.5Hz during a down sweep at a frame

acceleration of 1g. The corresponding bandwidth was measured at approximately 4.5Hz. The figure of merits show that the system has a power density ( $0.48\text{mWcm}^{-3}$  at 1g) and a normalised power integral density ( $11.9\text{kgm}^{-3}$  at 1g) that is comparable to in-plane electromagnetic and 3D printed systems found in the literature.

### Acknowledgements

This work is financially supported by Science Foundation Ireland (SFI) Principal Investigator (PI) project on 'Vibrational Energy Harvesting' grant no. SFI-11/PI/1201.

**Table 6: Comparison of different systems in the literature**

The necessary information for an extensive comparison is limited and where necessary data has been derived empirically from the figures supplied in the publications

Ref.	Type <sup>(1)</sup>	CAT <sup>(2)</sup>	Volume [cm <sup>3</sup> ]	Acceleration [g = 9.81ms <sup>-2</sup> ]	Frequency [Hz]	Bandwidth [Hz]	Power [mW]	Power Density [mWcm <sup>-3</sup> ]	Normalised Power Integral Density [kg m <sup>-3</sup> ]
[24]	ES	MEMS	0.015 <sup>(3)</sup>	1	625	14.5	0.228x10 <sup>-3</sup>	15.2x10 <sup>-3</sup>	1.72
[25]	ES	MEMS	0.015 <sup>(3)</sup>	1	575	535	3.4x10 <sup>-3</sup>	0.227 x10 <sup>-3</sup>	1008
[26]	ES	MEMS	0.042	0.707	150	40	2.2x10 <sup>-3</sup>	52.4x10 <sup>-3</sup>	39.5
[27]	PZ	MEMS	0.015 <sup>(9)</sup>	1	626.5	-	4.5x10 <sup>-3</sup>	0.305 <sup>(10)</sup>	-
[27]	PZ	MEMS	0.026	1	163.5	-	23.14x10 <sup>-3</sup>	0.89	-
[28]	PZ	MEMS	0.005	0.45	2	-	2.27x10 <sup>-6(4)</sup>	0.45x10 <sup>-3</sup>	-
[23]	EM	MESO	1	0.23	61	8	2.114x 10 <sup>-3</sup>	2.114x10 <sup>-3</sup>	2.52
[33]	EM	MESO	4.4	0.5	45.2	1.4	150 x 10 <sup>-3</sup>	0.034	1.49
[32]	EM	MEMS	0.09	0.75→3.75	290	20 @ 3.75g	0.2→2.6 x 10 <sup>-3</sup>	2.2→29 x10 <sup>-3</sup>	-
[32]	EM	MACRO	26	2.1→11.2	65	45 @ 2.1g	11.7→263	0.45→10	-
[31]	EM	MEMS	0.1	0.45	8080	286	148x10 <sup>-6</sup>	1.48x10 <sup>-3</sup>	16.5
[34]	EM	MESO	5.3	0.2→5	75	-	0.7x10 <sup>-3</sup> →1.04	0.13x10 <sup>-3</sup> →0.2	-
This Work	EM	MESO	6 <sup>(5)</sup>	0.1	147→152 <sup>(6)</sup>	1→4.5 <sup>(6,7)</sup>	24x10 <sup>-3(8)</sup>	0.004 <sup>(7)</sup>	5.3 <sup>(7)</sup>
				0.5			0.7 <sup>(8)</sup>	0.12 <sup>(7)</sup>	6.95 <sup>(7)</sup>
				1			2.9 <sup>(8)</sup>	0.48 <sup>(7)</sup>	11.9 <sup>(7)</sup>

(1) ES – Electrostatic, PZ –Piezoelectric, EM-Electromagnetic, (2) CAT = Category: MEMS <0.1cm<sup>3</sup>; MESO <10cm<sup>3</sup>; MACRO >10cm<sup>3</sup> (3)Chip size = 1cm<sup>2</sup> and device layer = 150µm (4) instantaneous power (5) active volume (6) for both up and down sweeps (7)bandwidth is that of high energy branch at the bandwidth power level of the low energy branch (8) down sweeps values (9)estimated volume (10) reported PD

### References

[1] D. Lammers, "Fabs in the Internet of Things Era," *Nanochip Fab Solutions - Applied Materials*, vol. 8, pp. 20-23, 2013.

[2] B. Grynol, "Disruptive Manufacturing: The effects of 3D printing (Deloitte)," pp. 1-16.

[3] M. Cotteleer, J. Holdowsky, and M. Mahto, "The 3D opportunity primer: The basics of additive manufacturing," *A Deloitte series on additive manufacturing*, pp. 1-18, 2013.

[4] V. A. Lifton, G. Lifton, and S. Simon, "Options for additive rapid prototyping methods (3D printing) in MEMS technology," *Rapid Prototyping Journal*, vol. 20, pp. 403-412, 2014.

[5] ExOne, "innovent datasheet," p. 1, 2015.

[6] ExOne, "Exerial datasheet," p. 1, 2015.

[7] S. Ziemian, M. O. Constance, and W. Ziemian, "Tensile and Fatigue behaviour of layered acrylonitrile

butadiene styrene," *Rapid Prototyping Journal*, vol. 21, pp. 270-278, 2015.

[8] T. Letcher and M. Waytashek, "Material Property Testing of 3D-printed specimen in PLA on an entry-level 3D printer," presented at the Proceedings of the ASME 2014 International Mechanical Engineering Congress & Exposition, Montreal, Quebec, Canada, 2014.

[9] J. Kotlinski, "Mechanical Properties of Commercial Rapid Prototyping Materials," *Rapid Prototyping Journal*, vol. 20, pp. 499-510, 2014.

[10] C. Ziemian, M. Sharma, and S. Ziemian, "Anisotropic Mechanical Properties of ABS Parts Fabricated by Fused Deposition Modelling," in *Mechanical Engineering*, ed: InTech, 2012, pp. 159-179.

[11] Stratays, "ABSplus-P430 - Production grade thermoplastics for design series 3D printers," pp. 1-2, 2014.

[12] Stratays, "FDM Nylon 12 - Production Grade thermoplastic for Fortus 3D production systems," pp. 1-2, 2015.

- [13] Stratasy, "PC (polycarbonate) Production-grade thermoplastic for Fortus 3D production systems," pp. 1-2, 2015.
- [14] NatureWorks, "Ingeo Biopolymer 4043D Technical Data Sheet - 3D printing monofilament - General Purpose Grade," ed, pp. 1-4.
- [15] D. Mallick, P. Podder, and S. Roy, "Wideband electromagnetic energy harvesting from ambient vibrations," presented at the AIP Conference Proceedings - 1665, 2015.
- [16] Z. Hadas, V. Singule, and C. Ondrusek, "Design of Energy Harvesting Generator Base on Rapid Prototyping Parts," presented at the 13th International Power Electronics and Motion Control Conference (EPE-PEMC 2008), 2008.
- [17] O. Rubes, J. Smilek, and Z. Hadas, "Development of Vibration Energy Harvester Fabricated by Rapid Prototyping Technology," presented at the 16th International Conference on Mechatronics - Mechatronika (ME), Brno, 2014.
- [18] B. J. Bowers and D. P. Arnold, "Spherical Magnetic Generators for Bio-Motional Energy Harvesting," presented at the PowerMEMS + microEMS conference, Sendai, Japan, 2008.
- [19] J. Heit, D. Christensen, and S. Roundy, "A vibration energy harvesting structure, tunable over a wide frequency range using minimal actuation," presented at the Proceedings of the ASME 2013 Conference on Smart Materials, Adaptive Structures and Intelligent Systems, Snowbird, Utah, USA, 2013.
- [20] P. Pillatsch, L. M. Miller, E. Halvorsen, P. K. Wright, E. M. Yeatman, and A. S. Holmes, "Self-tuning behaviour of a clamped-clamped beam with sliding proof mass for broadband energy harvesting," presented at the PowerMEMS conference, 2013.
- [21] S. C. Chang, F. M. Yaul, A. Dominguez-Garcia, F. O'Sullivan, D. M. Otten, and J. H. Lang, "Harvesting Energy From Moth Vibrations During Flight," presented at the PowerMEMS conference in, Washington DC, USA, 2009.
- [22] X. Wu and D. W. Lee, "A high-efficient broadband energy harvester based on non-contact coupling techniques for ambient vibrations," presented at the IEEE MEMS conference, Estoril, Portugal, 2015.
- [23] E. Baker, T. Reissman, F. Zhou, C. Wang, K. Lynch, and C. Sun, "Microstereolithography of three dimensional polymeric springs for vibration energy harvesting," *Smart Materials Research, Hindawi Publishing Corporation*, vol. 2021, p. 9, 2012.
- [24] Q. Fu and Y. Suzuki, "In-plane gap-closing MEMS vibration electret energy harvester on thick box layer," presented at the Transducers conference, Anchorage, Alaska, 2015.
- [25] S. D. Nguyen, E. Halvorsen, and I. Paprotny, "Bistable spring for wideband microelectromechanical energy harvesters," *Applied Physics Letters*, vol. 102, pp. 1-4, 2013.
- [26] R. Guillemet, P. Basset, D. Galayko, F. Cottone, F. Marty, and T. Bourouina, "Wideband MEMS Electrostatic Vibration Energy Harvesters based on gap-closing interdigitated combs with a trapezoidal cross section," presented at the IEEE MEMS conference, Taipei, Taiwan, 2013.
- [27] S. Nadig, S. Ardanuc, and A. Lal, "Monolithic 2-axis in-plane PZT lateral bimorph energy harvester with differential output," presented at the IEEE MEMS conference, Estoril, Portugal, 2015.
- [28] J. L. Fu, Y. Nakano, L. D. Sorenson, and F. Ayazi, "Multi-axis AlN-on-silicon vibration energy harvester with integrated frequency-upconverting transducers," presented at the IEEE MEMS conference, Paris, France, 2012.
- [29] S. Roundy and E. Takahashi, "A planar electromagnetic energy harvesting transducer using a multipole magnetic plate," *Sensors and Actuators A: Physical*, vol. 195, pp. 98-104, 2013.
- [30] S. Chae, S. Ju, Y. Choi, S. Park, S. Lee, H. Lee, *et al.*, "Electromagnetic Vibration Energy Harvester Using Springless Proof Mass and Ferrofluid as lubricant," presented at the PowerMEMS conference, 2013.
- [31] S. Kulkarni, E. Koukharenko, R. Torah, J. Tudor, S. Beeby, T. O'Donnell, *et al.*, "Design, fabrication and test of integrated micro-scale vibration -based electromagnetic generator," *Sensors and Actuators A: Physical*, vol. 145-146, pp. 336-342, 2008.
- [32] Q. Zhang and K. E. S., "Vibration Energy Harvesting Based on Magnet and Coil Arrays for Watt-Level Handheld Power Source," *Proceedings of the IEEE*, vol. 102, pp. 1747-1761, 2014.
- [33] D. Zhu, S. Beeby, J. Tudor, and N. Harris, "Vibration energy harvesting using the Halbach Array," *Smart Materials and Structures*, vol. 21, pp. 1-11, 2012.
- [34] Q. Zhang, Y. Wang, L. Zhao, and E. Kim, "Integration of microfabricated low resistance and thousand turn coils for vibration energy harvesting," *Journal of Micromechanics and Microengineering*, vol. 26, pp. 1-10, 2016.
- [35] C. B. Williams, C. Shearwood, M. A. Harradine, P. H. Mellor, T. S. Birch, and R. B. Yates, "Development of an electromagnetic micro-generator," *IEE Proceedings - Circuits, Devices and Systems*, vol. 148, pp. 337-342, 2001.
- [36] P. Xu, Y. Jingjun, Z. Guanghua, and B. Shusheng, "The stiffness model of leaf-type isosceles-trapezoidal flexural pivots," *Journal of Mechanical Design*, vol. 130, pp. 1-6, 2008.
- [37] P. Xu, Y. Jingjun, Z. Guanghua, B. Shusheng, and Y. Zhiwei, "Analysis of Rotational Precision for an Isosceles-Trapezoidal Flexural Pivot," *Journal of Mechanical Design*, vol. 130, pp. 1-9, 2008.
- [38] D. Mallick, A. Amann, and S. Roy, "Interplay between electrical and mechanical domains in a high performance nonlinear energy harvester," *Smart Materials and Structures*, vol. 24, pp. 1-9, 2015.
- [39] D. Mallick, A. Amann, and S. Roy, "A nonlinear stretching based electromagnetic energy harvester on FR4 for wideband operation," *Smart Materials and Structures*, vol. 24, pp. 1-14, 2015.
- [40] P. Podder, A. Amann, and S. Roy, "A bistable electromagnetic micro-power generator using FR4-based folded arm cantilever," *Sensors and Actuators A: Physical*, vol. 227, pp. 39-47, 2015.

- [41] G. Hatipoglu and H. Urey, "FR4-based electromagnetic energy harvester for wireless sensor nodes," *Smart Materials and Structures*, vol. 19, pp. 1-11, 2010.
- [42] Anonymous, "The Free Beginner's Guide to 3D printing," in *3dprintingindustry.com* ed, pp. 1-77.
- [43] P. Constantinou, P. H. Mellor, and P. Wilcox, "Model of an electromagnetic vibration generator," presented at the Proceedings of the 41st International Universities Power Engineering Conference, Newcastle upon Tyne, UK, 2006.
- [44] S. Priya and D. J. Inman, *Energy Harvesting Technologies*, 1 ed.: Springer, 2009.
- [45] S. D. Nguyen and E. Halvorsen, "Analysis of vibration energy harvesters utilizing a variety of nonlinear springs," presented at the PowerMEMS conference, 2010.